MIT Libraries | DSpace@MIT

MIT Open Access Articles

Three-Dimensional Imaging of Electrospun Fiber Mats Using Confocal Laser Scanning Microscopy and Digital Image Analysis

Massachusetts Institute of Technology

Three-Dimensional Imaging of Electrospun Fiber Mats Using Confocal Laser Scanning Microscopy and Digital Image Analysis

Looh Tchuin (Simon) Choong[1,‡], Peng Yi[1,2,‡] and Gregory C. Rutledge[1,*]

[1]Department of Chemical Engineering, Massachusetts Institute of Technology, Cambridge, MA 02139, USA

[2]Current Address: Department of Materials Science and Engineering, Johns Hopkins University, Baltimore, MD 21218, USA

Authors email addresses:

Looh Tchuin (Simon) Choong (schoong@mit.edu)

Peng Yi (pengyi@jhu.edu)

Gregory C. Rutledge (rutledge@mit.edu)

Corresponding Author

[*] To whom correspondence should be addressed. Phone number: 617-253-0171

Author Contributions

[‡] These authors contributed equally to this work.

Abstract

Confocal laser scanning microscopy with fluorescent markers and index matching has been used to collect three-dimensional (3D) digitized images of electrospun fiber mats and of a borosilicate glass fiber material. By embedding the fluorescent dye in either the material component (fibers) or pore space component (the index matching fluid), acquisitions of both positive and negative images of the porous fibrous materials are demonstrated. Image analysis techniques are then applied to the 3D reconstructions of the fibrous materials to extract important morphological characteristics such as porosity, specific surface area, distributions of fiber diameter and of pore diameter, and fiber orientation distribution; the results are compared with other experimental measurements where available. The topology of the pore space is quantified for an electrospun mat for the first time using the Euler-Poincaré characteristic. Finally, a method is presented for subdividing the pore space into a network of cavities and the gates that interconnect them, by which the network structure of the pore space in these electrospun mats is determined.

Keywords: Confocal laser scanning microscopy (CLSM), 3D imaging, porous media, nonwovens, electrospinning, network model

1   Introduction

The characterization of porous media is of critical importance in a wide variety of disciplines and applications, including mathematics, soil physics, petroleum engineering, biomedical devices, and materials design [1-3]. It is often desired to understand the relation between the structural and the functional properties, e.g., fluid filtration properties, of the porous media. On the one hand, knowing this relation enables the calculation of functional properties based on structural information; on the other hand, it can facilitate the design of porous materials for desired functional properties. Given the full 3-dimensional (3D) structure of the porous medium, for example, computer simulations can be used to solve Stokes' equation for the calculation of various static and dynamics properties of a fluid in the porous medium [4-6]. This type of simulation, however, is computationally expensive. Alternatively, a small number of morphological metrics characterizing the porous medium can be identified that control a particular functional behavior. One such example of this approach is the well-known Kozeny-Carman (KC) model for permeability of a porous medium [7, 8], for which the key structural parameters are the porosity, tortuosity and the specific surface area of the porous material. Although the latter approach is, by construction, a simplification of the full relationship between structure and function, models such as the KC model are still widely appreciated for their analytical tractability and ease of interpretation. A significant problem often encountered with such models, however, is the ambiguity with which the controlling structural parameters are defined and measured experimentally.

The network model is a compromise between the two approaches described above [9]. It was proposed over half century ago, but only recently has received more attention with the advancement of better imaging techniques and increased computer power. The network model treats fluid passages in porous media as (usually, cylindrical) channels that meet at junction points on a lattice. It has been used to predict static properties of fluids in porous media like sandstones [10]. In addition, combined with Lattice-Boltzmann simulations [11], the network model can also be used to calculate the dynamical properties of fluids.

The fibrous materials evaluated in this work were obtained by electrospinning. Electrospinning is a process that readily produces fibers with diameters in the range of 100 nm to 10 μm. The fibers, and the nonwoven mats comprising them, have great potential in a wide variety of applications, such as tissue engineering [12, 13], filtration [14], and sensors [15, 16]. This promise is attributed to several important properties of electrospun mats: small fiber diameter, high surface area per unit mass, high porosity and small pore size [17]. The bi-continuous nature of the fiber and pore spaces should also be important for filtration and membrane applications, through the mechanical integrity provided by the interconnected fiber component and the robustness against fouling, for example, provided by an interconnected pore space component. The size and orientation of fibers within a plane on the surface of the electrospun membrane are typically characterized by image analysis of 2-dimensional micrographs of the electrospun mats obtained by scanning electron microscopy (SEM). However, relatively little is known about fiber orientation or curl in the third (or thickness) dimension of the membrane [18], or the variation of fiber packing with depth. Efforts to extract information about the third dimension from 2D micrographs have been limited [19].

Total porosity of the membrane can be determined gravimetrically or by intrusive methods like mercury porosimetry. However, due to the large compliance of electrospun membranes, determination of the pore size distribution is complicated by deformation of the sample when pressure is applied during the measurement [20]. Also, analysis of mercury porosimetry data, like that of many other techniques used to characterize porous materials, requires a pore shape model to convert pressure to a dimension (e.g. diameter), for which an overly-simplistic cylindrical geometry is usually employed; the cylindrical pore model is especially inappropriate for fibrous materials like electrospun mats, as is readily apparent from inspection of a typical SEM micrograph, such as the one shown in Fig.1. Capillary flow porometry and bubble point measurements generally require lower pressures to characterize the pore sizes of electrospun membranes, but still require a pore shape model and are biased towards sampling of constrictions within channels that span the dimension of the sample (due to the "ink-bottle effect" [20]). Dead-end pore volumes are not measured at all [21], but are not likely to be significant for the materials considered in this work. It is expected that the inter-fibrillar spaces are far more complex than can adequately be represented by such indirect measures and simplistic models. Sampson proposed a relatively simple analytical model for pore radii in isotropic, near-planar stochastic networks of rod-like fibers, and predicted highly anisotropic pore shapes [22, 23]. The interconnectivity of the pore space has yet to be characterized experimentally.

To remedy these problems, the technique developed in this work measures and digitizes the three-dimensional (3D) structure of electrospun fibrous materials, so that a more thorough and accurate analysis of both the material and the pore space is possible. With modern imaging

techniques, it has become possible to extract the full 3D structure from porous samples and to test those metrics that may be controlling in models for the functional properties of porous media. However, such imaging techniques are often tedious, destructive and/or expensive. In this work we demonstrate a simple, efficient, nondestructive method for obtaining 3D images of porous fibrous materials, and develop the necessary analysis tools to extract a number of morphological and topological properties of the nonwoven material.
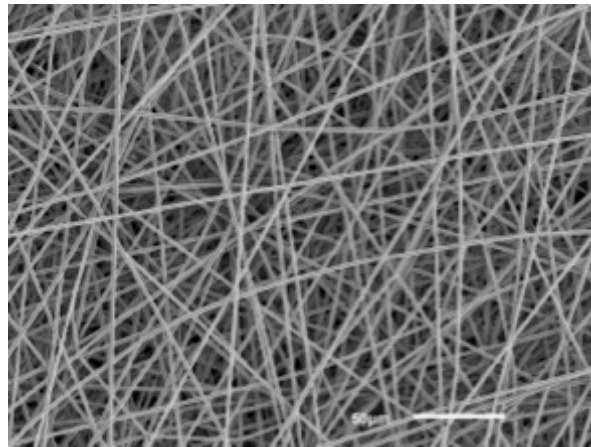

Fig.1 A typical scanning electron microscopy image of electrospun fiber mats. The sample is made of poly(trimethyl hexamethylene terephthalamide) (PA 6(3)T) fibers that are 2.08 ± 0.15μm in diameter; see text for details

Several methods [24] have been previously used to obtain the 3D structure of porous media; these can be categorized as destructive or non-destructive. The destructive methods involve serial sectioning and 2D imaging of each section of the sample. Although these methods are often tedious, the in-plane (x-y) resolution can be very good, depending on the imaging technique used, e.g. ~0.2 nm for transmission electron microscopy (TEM) and ~10 nm for scanning electron microscopy (SEM). The depth (z-direction) resolution depends on how thinly

the samples can be sectioned. Sectioning done by focused ion beam (FIB) or glass/diamond knives typically has in-plane and depth resolutions of 15 nm and ~0.05-0.1μm, respectively [5, 25]. These techniques have been applied to soil [5], microporous membranes [26], and electrospun mats [27] .

Non-destructive methods are required when the samples are also used for other analyses in addition to 3D imaging. For example, simultaneous micro-computed tomography (micro-CT) and micromechanical testing have been used to study the behavior of tissue scaffolds under compression [3], the structural change of a strained nonwoven papermaker felt [28], and the mechanical properties of sandstone [29]; while the permeabilities of sandstones and packed bed columns have been studied by imaging the water in the void space using magnetic resonance imaging (MRI) [1, 6]. While micro-CT images the porous medium itself, MRI images the void space within (e.g. water). The resolution of micro-CT typically ranges from 1 to 50 μm [24] and the best MRI resolution is on the order of 10 μm [1].

Confocal laser scanning microscopy (CLSM) is a nondestructive imaging technique based on optical microscopy that offers in-plane optical resolution down to about 0.2 μm. The depth optical resolution is generally proportional to and about three times that of the in-plane resolution. The optical resolution (d_{om}) is related to the incident wavelength (λ) and the numerical aperture (NA), by the equation $d_{om}=0.61\lambda/1.31NA$ [30]. NA=1.4 for the objective used in this work. CLSM was first demonstrated on electrospun mats by Bagherzadeh et al. [27]. However, the technique employed by Bagherzadeh et al. is limited to imaging only the first few

7

microns at the surface of the specimen, due to the scattering of light by the specimen, so that 3D reconstruction is not possible.

In this work, we employed a refractive index-matching fluid to suppress scattering. By suppressing scattering, we can demonstrate non-destructive imaging and full 3D reconstruction of porous fibrous materials up to depths of ~50 μm for the first time. We differentiate between two types of imaging, which we call "positive" imaging and "negative" imaging. In positive imaging, the contrast agent (a fluorescent dye) is added to the material itself during fabrication; in negative imaging, the contrast agent is added instead to the index matching fluid. As demonstrated here, the negative imaging technique can be applied to porous materials that have not been specifically formulated for imaging purposes. Finally, we use 3D image analysis algorithms to extract several important structural metrics of electrospun fiber materials, including several that are not currently achievable by other means. We propose a network model comprising cavities and gates to characterize the pore space of the material.

2 Experimental

2.1 Materials

Poly(trimethylhexamethylene terephthalamide) (PA 6(3)T) was purchased from Scientific Polymer Products, Inc. N,N-dimethyl acetamide (DMAc), formic acid (FA), perylene, benzene and iodobenzene were purchased from Sigma–Aldrich and used as received. F1300 fluorescein was purchased from Invitrogen. Commercial Grade C borosilicate glass fiber (BGF) filter (1.1 μm nominal pore size, C2500) was purchased from Sterlitech.

2.2   Fabrication

Undyed nanofiber mats were fabricated by electrospinning from organic polymer solutions using a parallel-plate geometry described previously [31]. Briefly, two aluminum plates, each 12 cm in diameter, were positioned one above the other, with the spinneret mounted in the center of the top plate and a tip-to-collector distance of 25-40 cm. A high voltage power supply (Gamma High Voltage Research, ES40P) was used to apply an electrical potential of 23-26 kV to the polymer solution and the top plate, while the bottom plate (collector) was grounded. The spinneret consisted of a stainless steel capillary tube (1.6 mm OD, 1.0 mm ID) (Upchurch Scientific). A digitally controlled syringe pump (Harvard Apparatus, PHD 2000) was used to control flow rate in the range of 0.01-0.02 mL min^{-1}. To render the fibers fluorescent, 0.1 wt% F-1300 dye was first dissolved in DMAc before adding the PA 6(3)T to form the polymer solution with a concentration of 34 wt%, which was then used for electrospinning as described.   At this concentration, the dye does not have any apparent effect on the formation of fibers.

2.3   Characterization

2.3.1   Porosity and BET analysis

The porosity ε_g was measured gravimetrically, i.e. from the basis weight (m) and thickness (t) of the mat, and the bulk density of the polymer (ρ_f), according to the equation $\varepsilon_g = \left(1 - m/t\rho_f\right)$. Due to the compressible nature of electrospun mats [31], the thickness measurement is prone to measurement error. To improve reproducibility, the mass was determined independently for five 1 cm diameter samples taken from each mat, and the thickness of each sample was measured

using an adjustable measuring force digital micrometer (Mutitoyo, Model CLM 1.6"QM) with a contact force of 0.5N.

The surface area of samples was measured using a Physisorption Analyzer (Micromeritics, ASAP 2020) with krypton as the test gas and Brunauer-Emmett-Teller (BET) theory to obtain the mass-specific surface area from the adsorption isotherm. The mass-specific surface area was converted to volume-specific surface area by multiplying with the density of the bulk material.

2.3.2   2-D Fiber Diameter and Orientation

The average fiber diameter of the electrospun fiber mats was calculated from the measurement of 30 to 50 fibers in images taken with a scanning electron microscope (SEM, JEOL-JSM-6060). SEM images were also taken at a lower magnification as shown in Fig.1 for the analysis of fiber orientation. The analysis was performed using an algorithm based on the orientation of ''simple neighborhoods'', as proposed by Jähne [32]. The derivatives of the pixel intensity along the x- and y- directions form a structure tensor, of which one of the eigenvectors represents the local orientation of the fibers. An orientation angle, ϕ, with respect to the x-axis can thus be obtained. The orientation factor f is computed from the fiber orientation distribution, $\psi(\phi)$, according to Eq. (1) [33].   The value of f is bounded between 0 (unidirectional) and $2/\pi$ (planar random orientation):

$$f = \int_0^\pi \int_0^\pi \left|\sin(\phi' - \phi)\right| \psi(\phi')\psi(\phi)d\phi'd\phi. \tag{1}$$

2.3.3   Capillary flow porometry

The bubble point diameter, mean flow pore diameter, and pore size distribution were measured by capillary flow porometry, performed by Porous Materials Inc (PMI, Ithaca, NY). In this technique, the flow rate of gas through the porous material is measured as a function of pressure drop across the membrane, both for the dry membrane and for the membrane fully infiltrated with a wetting fluid (Galwick, surface tension γ=15.9 dynes cm^{-1}), $F_{dry}(\Delta P)$ and $F_{wet}(\Delta P)$, respectively. Upon increasing gas pressure, the point at which the first flow of gas through the wetted material is detected is called the bubble point, corresponding to channels through the material with the largest "throat", or narrow point in the channel. Upon further increasing pressure, additional channels open up, until the wetting liquid is completely removed from the channels that span the sample, and the flow rate of gas again approaches that of the dry material. The pressure drop at which $F_{wet}(\Delta P)/F_{dry}(\Delta P) = 1/2$ is associated with the "mean flow pore diameter". It is conventional to convert the measured pressure to pore diameter (s) by assuming that the Young-Laplace equation for a cylindrical pore applies: $s = 4B\gamma\cos\theta/\Delta P$, where the contact angle $\theta = 0°$ is assumed for a wetting fluid like Galwick, and B is a shape factor for the pores. B=1 for cylindrical pores; for fibrous media, PMI assumes a value of B=0.715. The "capillary flow pore size distribution" ($g(s)$) was estimated by differentiating with respect to pressure the ratio of gas flow rate through a wet sample to that through a dry sample, and converting to pore diameter using the Young-Laplace equation, i.e. $g(s) = -\left(d\left[F_{wet}/F_{dry}\right]\big/d\Delta P\right)\left(d\Delta P/ds\right)$.

2.4   Refractive index matching

For imaging purposes, all samples were impregnated with a fluid designed to match the refractive index (*n*) of the material (e.g., PA 6(3)T, *n*=1.566), in order to minimize the scattering of the laser as it travels deeper into the mats. The use of index matching is essential to the acquisition of 3D data sets, reaching depths of 50-100 μm into the sample. The design of the index matching fluid (IMF) is accomplished using a miscible pair of fluids having different indices of refraction, one higher and the other one lower than the index of refraction of the material of interest. The fluids should be able to wet the material, but not dissolve or swell it. Benzene and iodobenzene were chosen to form the IMF used in this work. Their refractive indices are 1.501 and 1.62, respectively. The composition of the IMF was determined using the following equation [34]:

$$\frac{n_{12}^2 - n_1^2}{n_{12}^2 - 2n_1^2} = \phi_2 \frac{n_2^2 - n_1^2}{n_2^2 - 2n_1^2}, \tag{2}$$

where ϕ is the volume fraction; and the subscripts 1, 2 and 12 represent benzene, iodobenzene and the mixture of the two, respectively. The IMF for PA 6(3)T (refractive index n=1.566 [35]) contained 45.1 vol% benzene and 54.9 vol% iodobenzene, while the IMF for BGF (n=1.514 [36]) contained 89 vol% benzene and 11 vol% iodobenzene. The wettabilities of both benzene and iodobenzene were tested by putting a drop of each of these liquids onto the membranes. Both liquids were absorbed immediately, with zero contact angle, indicating good wettabilty. SEM images were taken before exposure to the IMF and again after the IMF evaporated; no changes in the morphologies of the membranes were observed.

2.5   3D Image Generation

The 3D structures of PA6(3)T mats and the BGF membrane were imaged using a confocal laser scanning microscope, CLSM (Zeiss LSM 700). A fluorescent dye was used for contrast, but the sample preparations for "positive" and "negative" imaging differed slightly. For positive imaging, in which the sample material itself is fluorescently dyed, F-1300 (a nonvolatile polar fluorescent dye) was added into the solvent used for electrospinning and subsequently incorporated uniformly into the fibers themselves; the concentration of dye in the fibers was about 2 mg g^{-1}. For negative imaging, in which the liquid that fills the pore space is fluorescently dyed, 0.1 wt% perylene (a non-polar dye) was first dissolved in benzene before mixing with iodobenzene; the perylene concentration in the final mixture for the imaging of PA6(3)T and BGF was 0.4 mg ml^{-1} and 0.78 mg ml^{-1}, respectively. To prevent the evaporation of the IMF, a cover slip was used, and the edges of the cover slip were sealed by lacquer (a clear nail polish). The samples used for imaging were cut to a size of approximately 5x5 mm^2.

An oil-immersion objective with a magnification of 63X was used to image the membranes. The immersion oil was designed for high magnification imaging, and has a refractive index of 1.518, which is the same as that of the cover slip. Since the laser intensity attenuates as it travels through the sample, the laser power for three depths, corresponding to the top, middle, and bottom of a sample, was optimized manually and the Spline Interpolation correction algorithm (Zeiss) was used to determine the appropriate laser intensity for all intermediate depths. The excitation wavelengths for F-1300 and perylene are 488nm and 405nm, respectively. The in-plane digital resolution (μm/pixel) was determined by the imaging area and the pixel resolution of the image (1024 x 1024); thus, the digital resolution is 0.1μm/pixel and 0.05μm/pixel for

images with areas of ~100 x 100 μm^2 and 53 x 53 μm^2, respectively. For the depth digital resolution i.e. pixel size in the z-direction, the focal plane was incremented by 0.2μm. With these parameters, acquisition of a complete, 3D image of 50 μm depth requires a total laser exposure time of about 30 min. Higher resolutions would require longer imaging times, which can result in photo bleaching of the dye. The resulting 3D images were reconstructed using Fiji, an open-source image processing package commonly used for biological image analysis [37].

3   3D image analysis of porous membranes

3.1   Preprocessing of 3D images

3D geometrical image analysis was performed using software developed in-house. The images comprise a 3D array of volume elements, or "voxels", whose values correspond to the gray scale intensity measured at each voxel. For the fluorescent imaging technique used in this work, the gray scale values are expected to cluster around two populations, corresponding to "material" and "pore space" voxels, respectively. Images collected in the negative imaging mode were inverted so that material voxels correspond to higher gray scale values for purposes of subsequent analysis.

Segmentation was performed using a simple thresholding method. For those samples where the gray scale distribution was bimodal, such segmentation is straightforward; the gray scale value corresponding to the local minimum between the two peaks is the natural choice for the cutoff value G_c to distinguish the material voxels from the pore space voxels. More advanced segmentation methods exist [32] and have been employed in the analysis of fibrous media, for

14

example, with micro-CT data on paper [38], where it may be desired to distinguish several different types of components. However, such methods often come with additional complexity. For example, the region-growing method [38] first requires a selection of "seeds" based on the gray scale distribution, followed by an additional criterion to determine "similarity" between a "seeded" region and a voxel under consideration. Thresholding is a single parameter method whose adequacy for the current application can be justified *a posteriori*, for example through validation against independent measurements of fiber diameter by SEM.

Notwithstanding the foregoing discussion, the fluorescent imaging technique employed in this work does incur some practical difficulties that complicate thresholding in some cases. One difficulty we encountered is that the brightness of the voxels generally decreases with increasing depth into the sample due to light absorption, even after application of the correction for laser power along the z-axis (*c.f.* 3D Image Generation). As a result, the gray scale distribution can shift with increasing depth, resulting in broadening of peaks in the gray scale distribution and loss of a clear separation between material and pore space populations if combined into a single overall distribution. To handle this case, we determine the function $G_c(z)$ separately for each slice of voxels at a depth z (a "z-slice"). To obtain a smooth function for $G_c(z)$, the gray scale distribution was averaged over layers about 10 μm thick, or 50 z-slices, which is larger than the typical diameter of the fibers. This smooth $G_c(z)$ function can then be used in 3D image analysis to apportion voxels to material or pore spaces slice by slice. A second complication, which is not unique to thresholding, is that we work with samples having small volume fractions of material or in which the material dimensions are near the optical resolution of the microscope; in such samples, it is difficult to resolve the material peak separately from the pore space peak. In these

special cases (only), if an experimental value of porosity is available, we select the gray scale cutoff G_c in the 3D image so that the volume fraction of voxels in the pore space peak equals the experimentally measured porosity.

3.2　Porosity (ε) and Surface Area (S) Measurement

After segmentation of the 3D image, porosity and interfacial surface area are readily determined by direct counting of voxels and voxel sides. The porosity ε of the membrane is calculated by counting the fraction of voxels whose gray scale value is less than G_c. The solidity, or solid (material) volume fraction, is simply equal to $1-\varepsilon$.

The interfacial area between solid material and pore space is calculated as the total area of voxel side surfaces that are shared by one material voxel and one pore space voxel. A number of images taken at different locations within the same sample are used to compute the means and the standard deviations of porosity and surface area. The specific surface area, defined as the total interfacial area divided by the total material volume, $S/V(1-\varepsilon)$, is related to the inverse of the characteristic dimension of the material, to within a shape factor B_S that is of order unity for simple material geometries. For example, in the case of samples comprising uniform, cylindrical fibers, the characteristic dimension is the fiber diameter d and $B_S = 4$; i.e., the specific surface area is equal to $4/d$.

3.3 Fiber and pore radius distributions

The size distributions of the material space and the pore space of a sample provide detailed information about the morphology of the two complementary spaces, from which common metrics such as the average fiber diameter or pore diameter are readily obtained. This analysis is performed by fitting spheres into the material space and the pore space, respectively. For this purpose, two radii, R_b and R_c, are defined in each space. The boundary radius R_b is the shortest distance between a voxel (i, j, k) and any voxel of the *opposite kind*, i.e., material or pore space, and measures how close this voxel is to the nearest interface. The covering radius, R_c, of a voxel (i, j, k) is defined as the largest boundary radius $R_{b,lmn}$ of any voxel (l, m, n) of the *same kind* such that the distance between voxel (l, m, n) and voxel (i, j, k) is smaller than $R_{b,lmn}$. In other words, R_c of a material voxel (i, j, k) is the radius of the largest sphere allowed in the material space that covers, or includes, (i, j, k). By this definition, R_c is always equal to or greater than R_b for any given voxel. Thus, every voxel in the 3D data set is characterized by its indices, gray scale value (or indicator value), boundary radius and covering radius: $(i, j, k, g$ or $I, R_b, R_c)$. Probability distributions $P(R_c)$ are obtained from the histograms of voxels with covering radius R_c in the material and pore spaces, respectively, and are commonly taken to be the volume-weighted distributions of the material and pore radii in geometrical analyses of porous media[39, 40]. For media comprising very high aspect ratio fibers, the volume-weighted distribution of material radii is equivalent to the area-weighted fiber radius distribution; the number distribution is obtained by dividing each element of the histogram by the square of radius,

$$P_n(r^{mater}) \propto P(R_c^{mater}) / (R_c^{mater})^2, \tag{3}$$

where r^{mater} is the fiber radius and the average fiber diameter becomes

$$d = 2\langle r^{mater} \rangle = \int P_n(r^{mater}) r^{mater} dr^{mater}. \tag{4}$$

17

Meanwhile, the volume distribution of the pore space, $P\left(R_c^{pore}\right)$, is understood to be the relevant

morphological property measured by mercury porosimetry [39], so the average pore radius by

this method is

$$s = 2\left\langle R_c^{pore} \right\rangle = \int P(R_c^{pore}) R_c^{pore} dR_c^{pore}.$$

(5)

The two radii, R_b and R_c, are closely related to two common morphology operations in image

processing, erosion and dilation [41]. For a given threshold, R_{th}, all the voxels with $R_b \geq R_{th}$

constitute the eroded space for a structural element consisting of a sphere of radius R_{th}; all the

points with $R_c \geq R_{th}$ constitute the dilated space for the same structural element. As illustrated in

Fig.2, the operation of erosion followed by dilation (called "opening") serves the purpose of

removing information with length scale smaller than R_{th} in a digital image.

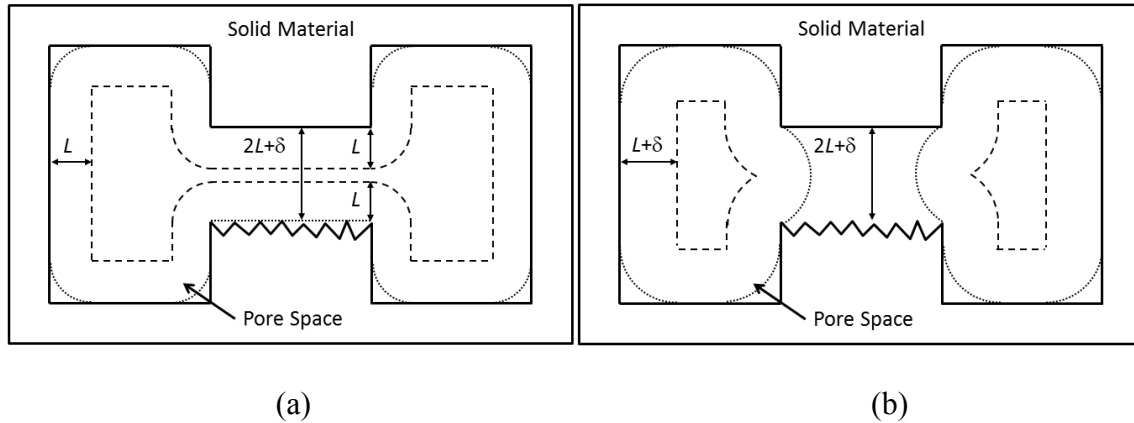(a)   (b)

Fig.2 Illustration of the eroded pore space ($R_b \geq R_{th}$, enclosed by dashed line) and the

corresponding dilated space ($R_c \geq R_{th}$, enclosed by dotted line) using two different R_{th} values: (a)

$R_{th}=L$; and (b) $R_{th}=L+\delta$. Note that the channel connecting the two larger pore spaces contributes

to both the eroded and dilated pore spaces when its radius is greater than or equal to L, but does

not contribute when its radius is less than $L+\delta/2$

18

3.4 Fiber orientation distribution

Another commonly measured morphological property of fibrous materials is the fiber orientation distribution. To compute the local fiber orientation, each material voxel is assigned a "voxel group" comprising all of the material voxels in it "neighborhood". This neighborhood is determined by a cutoff radius R_f, where R_f is taken to be larger than the upper bound of the fiber radius, as determined in the preceding section. Three eigenvalues and their corresponding eigenvectors are obtained by diagonalizing the gyration tensor of this voxel group. The eigenvector with the smallest eigenvalue, corresponding to the moment of gyration about that eigenvector, is the local direction of that fiber segment. Spherical coordinates θ and ϕ of this local direction are used to represent the orientation distribution of the fibers, where θ is the polar angle with respect to the z axis and ϕ is the azimuthal angle within the x-y plane. If desired, a similar calculation of local orientation could be applied to the pore space.

3.5 Pore space topology

Next, we characterize the topology of the pore space. Two voxels of the same kind (material or pore space) are topologically "connected" if they share one side surface, or if another voxel is connected to both of them. By this definition, if two voxels are connected, there must exist a path within the same space consisting only of connected voxels between them. Therefore the connectivity of a space (material or pore) is a measure of the number of ways that two arbitrary points within the space are connected. A "cluster" is defined as a group of mutually connected voxels of the same type. A small number of clusters in a unit volume implies a high connectivity,

and vice versa. Here, we evaluate the topological connectivity for the pore space, but we note that the operation could also be applied to the material space.

Given a measure X of the topological connectivity of the pore space, an operation such as erosion that alters the topology can be used to identify the characteristic length scale for the connecting elements. Comparing Fig.2 (a) and Fig.2 (b), if R_{th} is larger than the smallest R_b along the path connecting two pore space voxels, then that connection is broken as a result of the erosion operation. Therefore, the value of R_{th} for which dX/dR_{th} is maximal provides an objective measure of the characteristic size of "gates" or "channels" between larger aggregates, or "cavities", within the pore space. Different choices may be made for the topological metric X. Here, we employ the Euler-Poincaré characteristic, $\chi = N–C+H$, which is commonly used to quantify the connectivity within the pore space of porous materials [42]. This metric is illustrated by Fig.3, where N is the number of isolated clusters, C is the total number of redundant connections and H is the number of "holes". A redundant connection is one that can be cut without creating an additional isolated cluster. A hole is an aggregate of material completely surrounded by pore space, which can generally be neglected for real materials (H=0). Smaller χ values correspond to greater topological connectivity. The value of χ can be estimated using an integral geometric approach, described elsewhere [43]. This method has been used to determine the pore connectivity in soil samples, for example [44]. For purposes of comparison between samples, we use the specific Euler-Poincaré characteristic $\chi_v = \chi/V$ to characterize the topological connectivity X.
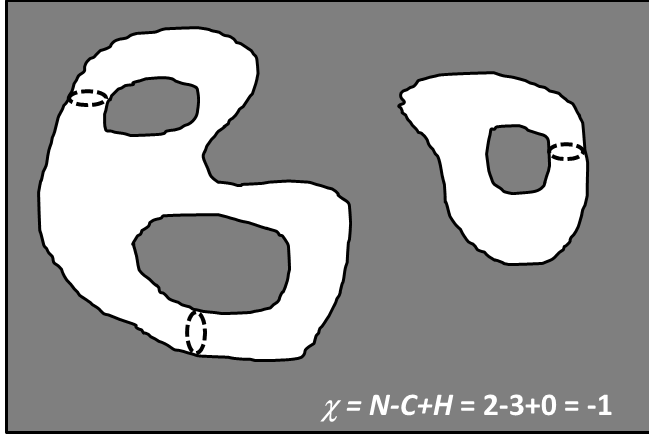
$$\chi = N\text{-}C\text{+}H = 2\text{-}3\text{+}0 = \text{-}1$$

Fig.3 An example of Euler-Poincaré characteristic, $\chi = N\text{–}C\text{+}H$, in two dimensions. Isolated clusters are shown in white. Redundant connections are identified by dashed ellipses. Adapted from Ref. [44]

3.6 The pore space network

In this section, we describe a means for characterizing the network structure of the pore space, comprising populations of "cavities" and "gates" that are mutually connected. A gate describes a group of pore space voxels that forms a connection between two or more cavities. As described in the previous section, the characteristic gate size is that for which the topology varies most rapidly with erosion, i.e. $d\chi_v/dR_{th}$ is maximal. To identify "gate" voxels, we define a lower bound, R_{th}^l, and an upper bound, R_{th}^u, that are chosen to bracket the characteristic gate size. Here, $\{R_{th}^l, R_{th}^u\}$ are identified by $\{R_{th}^{max}\text{–}\delta, R_{th}^{max}\text{+}\delta\}$, where R_{th}^{max} is the maximal value in the distribution of $d\chi_v/dR_{th}$ versus R_{th}, and δ expresses a range of R_{th} values for which the topology is most sensitive. The eroded space created by $R_b \geq R_{th}^l$ is just sufficient to retain the skeletal structure of the network, as illustrated in Fig.2 (a). Those voxels of this eroded space for which

21

$R_c \geq R_{th}^u$ are then identified as cavity voxels, while those for which $R_c < R_{th}^u$ belong to gates. In this way, the voxels in the eroded space are apportioned either to cavities or gates.

After all the voxels in the eroded pore space are identified as gate or cavity voxels, they are first clustered into distinct gates and cavities based on the connectivity of gate voxels and cavity voxels, respectively. Next, a gate (i.e. a cluster of gate voxels) is considered connected to a cavity (i.e. a cluster of cavity voxels) if any voxel in the former shares a side with any voxel in the latter. Two cavities are considered to be connected if they are both connected to a common gate. In this way, a network of cavities connected by shared gates can therefore be established. To characterize this network, we define the coordination number of each gate, N_{gate}, as the number of cavities that are connected to a given gate, and the coordination number of each cavity, N_{cav}, as the number of other cavities that are connected to a given cavity by any gate. It is commonly suggested that the pore size distribution measured by capillary flow porometry is indicative of the smallest diameters of channels (i.e. gates) connecting one side of the membrane to the other.

4   Results and discussion

4.1   Sample preparation and characterization

Table 1 summarizes the materials analyzed in this work. Groups A, B and C are all electrospun fiber mats of PA 6(3)T. Groups A and B are similar, except that fluorescent dye was added to the material component in Group A, and to the IMF in Group B. Group C is similar to Group A except that electrospinning conditions were changed to produce an average fiber diameter that is

about half as large. Group D is a borosilicate glass fiber material of comparable morphology, which serves as a commercially available standard. Fig.1 is an SEM image of a sample from Group B.

Table 2 summarizes the results of fiber and pore characterization of the samples from Groups A through D performed by the conventional methods of gravimetry, isothermal gas adsorption, analysis of SEM micrographs, and capillary flow porometry. Comparison of these results to those from the 3D imaging analysis is discussed in Section 4.4.

The samples sizes should be large enough to representative of the material being characterized. The minimum sample size, or representative volume element (RVE), depends on the specific morphological or physical property being analyzed. Deterministic and statistical measures of RVE have been proposed [45] and applied to porous media [46, 47]. A previous study of paper, another fibrous material, suggests that the dimension of the RVE is about 10 times larger than the characteristic length scale of the morphology (specifically, a covariance of gray scale) for purposes of both porosity and specific surface area measurement [47]. As evidenced by the data in Tables 1 and 2, the samples employed in this work easily satisfy this criterion.

Table 1 Summary of samples prepared for analysis.

Sample groups	Group A	Group B	Group C	Group D
Material	PA 6(3)T	PA 6(3)T	PA 6(3)T	Borosilicate glass

Solution concentration (wt%)	34	34	28	NA
Electrical potential (kV)	26	26	23	NA
Tip-to-collector distance (cm)	39	39	25	NA
Flow rate (mL min^{-1})	0.02	0.02	0.01	NA
Imaging method	Positive	Negative	Positive	Negative
Voxel size (μm)	0.1x0.1x0.2	0.1x0.1x0.2	0.05x0.05x0.2	0.1x0.1x0.2
Sample size (μm)	100x100x50	100x100x50	50x50x50	100x100x50
Number of samples	7	4	4	1

Table 2 Results of conventional characterization methods

	Group A	Group B	Group C	Group D
Porosity ε_g (gravimetric) (%)[a]	89.4 ± 0.9	89.5 ± 0.3	88.4 ± 0.5	90.9 ± 0.2
Specific surface area, S_{BET} (μm^{-1}) [b]	0.95 ± 0.05	0.87 ± 0.03	2.63 ± 0.03	5.16 ± 0.05
Fiber diameter, d_{SEM} (μm) [c]	2.57 ± 0.14	2.08 ± 0.15	1.13 ± 0.22	0.77 ± 1.11
Fiber orientation factor, f_{SEM} (SEM) [c]	0.53 ± 0.05	0.42 ± 0.09	0.53 ± 0.05	0.44± 0.07
Mean flow pore diameter, s_{mfp} (μm) [d]	11.5 ± 0.3	8.3 ± 0.3	4.5 ± 0.09	1.6 ± 0.3
Bubble point diameter, s_{bp}	13.61 ± 0.03	10.6 ± 0.2	5.6 ± 0.1	3.6 ± 0.6

(μm) [(d)]				

(a) Determined gravimetrically.

(b) Determined from adsorption isotherm using BET analysis

(c) Determined from SEM micrographs

(d) Determined from capillary flow porometry

4.2 Refractive Index Matching

Each sample was wetted with index-matching fluid (IMF) as described in Experimental. The effectiveness of index matching is illustrated in Fig.4, for both positive and negative imaging cases. The specimen appears transparent after addition of the wetting solution.
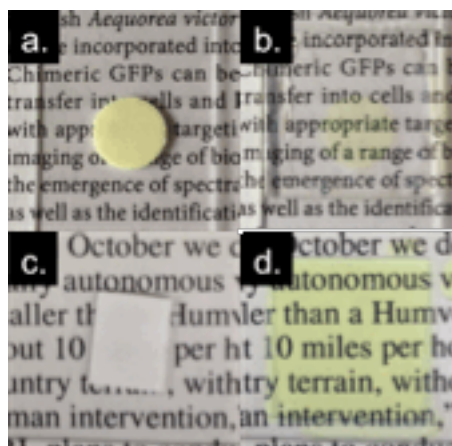
Fig.4 Impregnation of PA 6(3)T mats with a wetting fluid of 45.1 vol % benzene and the balance iodobenzene. (a,b) An electrospun mat of PA 6(3)T from Group A dyed with F1300, (a) as spun and (b) after wetting with the benzene-iodobenzene mixture. (c, d) An undyed electrospun mat of PA 6(3)T from Group B (c) as spun and (d) after wetting with the benzene-iodobenzene mixture containing perylene

4.3 3D Image Generation

Fig.5 shows 3D images for Groups A, B, C and D, reconstructed using Fiji. The sample sizes are approximately $100 \times 100 \times 50$ μm^3. For the positive imaging technique (Fig.5 (a) and (c)), the fibers are bright green (due to the F1300 dye) and the pore spaces are dark; for the negative imaging technique (Fig.5 (b) and (d)), the pore spaces are bright blue (due to perylene dye) and the fibers are dark. Careful examination of Fig.5 (b) or (d) reveals that the blue regions near the corners are darker than those near the center of the images. This is attributed to chromatic aberration, because the wavelength (405nm) used to excite perylene is near the lower limit (400nm) of wavelength for which the objective used is chromatically corrected, i.e. beams of different wavelength converge to the same focus point. Moreover, the transmittance of the objective is approximately 40% at a wavelength of 405nm (perylene), compared to approximately 75% at 488nm (F1300).
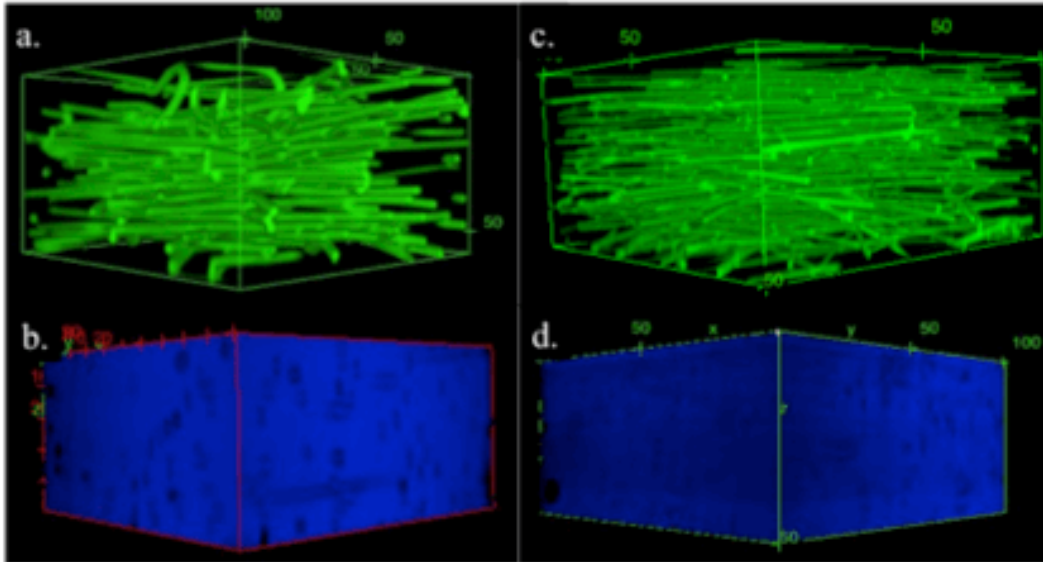
Fig.5 The 3D images reconstructed using Fiji. (a) Dyed electrospun PA 6(3)T mat from Group A; (b) undyed electrospun PA 6(3)T mat from Group B; (c) dyed electrospun PA 6(3)T from Group C; (d) commercial BGF membrane

4.4 3D Image Analysis

4.4.1 Porosity and Specific Surface Area

The gray scale distributions of seven images from Group A (positive imaging) are plotted in Fig.6 (a). Depending on the imaging conditions, as well as spatial variations in the porous material, the gray scale distributions are different for different sample images. Therefore the gray scale cutoff, G_c, also differs for each sample image; their values range from 15 to 83. Dividing each sample into several sections in the z-direction, G_c is found to be a smooth function of z, as illustrated by the first inset in Fig.6 (b) for one sample. The second inset in Fig.6 (b) shows the variation in estimated porosity as a function of sample depth, which confirms that the porosity is essentially constant in these materials on the 10 μm length scale. Fig.6 (c) shows one

27

of the reconstructed images, based on which we analyze the geometrical properties. Similar

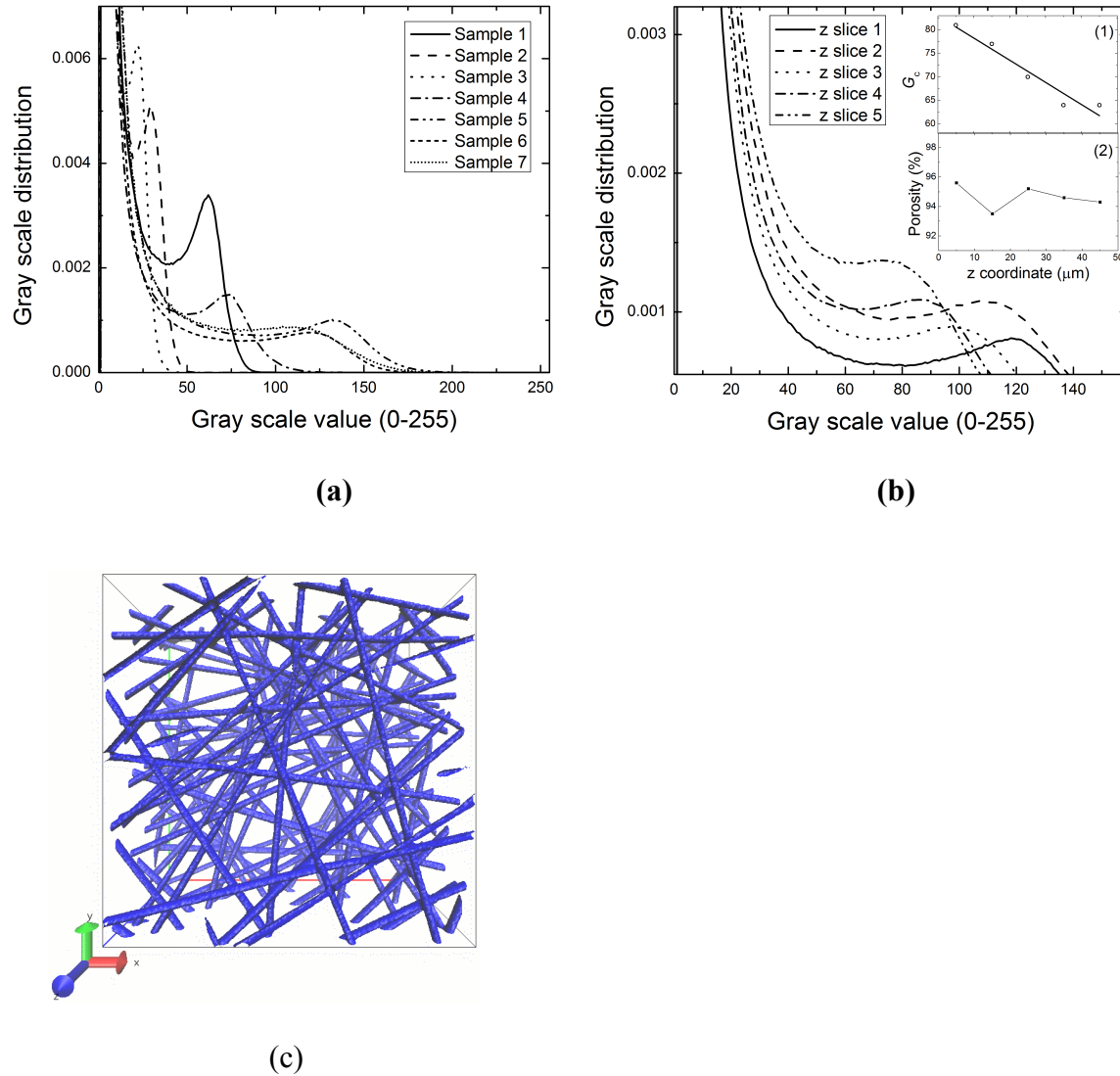results for image Group B (negative imaging) are shown in Fig.7.

(a)

(b)

(c)

Fig.6 (a) Gray scale distributions of sample images in Group A. (b) The gray scale distributions

for each of five z-slices from Sample #7 in Group A; inset (1) shows the cutoff function $G_c(z)$

versus z for this sample (with linear fit), and inset (2) shows the porosity versus z for this sample.

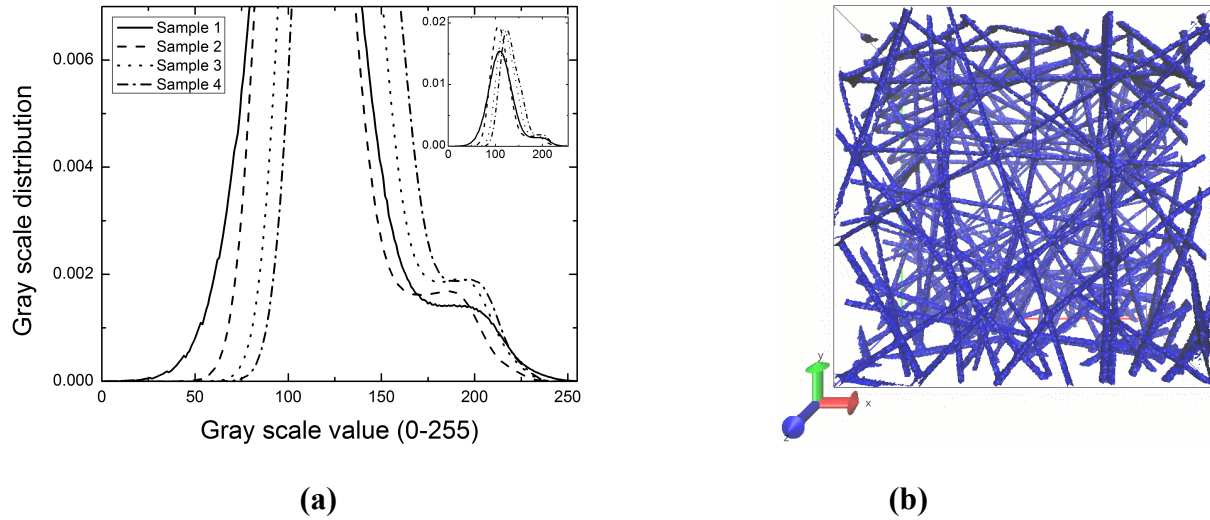(c) A reconstructed image of Sample #7 in Group A

Fig.7 (a) Gray scale distributions of sample images in Group B. (inset): the same data as the main plot, showing the full height of the gray scale distributions. (b) A reconstructed image of Sample #3 in Group B

Following the procedure described in Section 3.2, the porosities (ε) and specific surface areas (S) obtained for Groups A and B using the 3D image analysis of the CLSM data set are shown in Table 3, along with other results of the 3D CLSM data analysis. The porosities obtained for Groups A and B are nearly identical, which confirms the correspondence between positive and negative imaging methods. The porosities of these materials as determined gravimetrically (ε_g) are only slightly lower, at 89.4 ± 0.9% and 89.5 ± 0.3%. The difference between the two methods is attributed to the compressibility of the mats [31], which affects the values determined gravimetrically, since the thickness of the mat is measured using a micrometer at a fixed force of 0.5 N.

The gray scale distribution for BGF, Group D, is shown in Fig.8; the distribution for PA 6(3)T Group C was similar. In contrast to Groups A and B, Groups C and D do not exhibit clear bimodal gray scale distributions; for these groups, the porosity was determined gravimetrically and used to fix G_c. A reconstructed image of BGF from Group D is also shown in Fig.8.
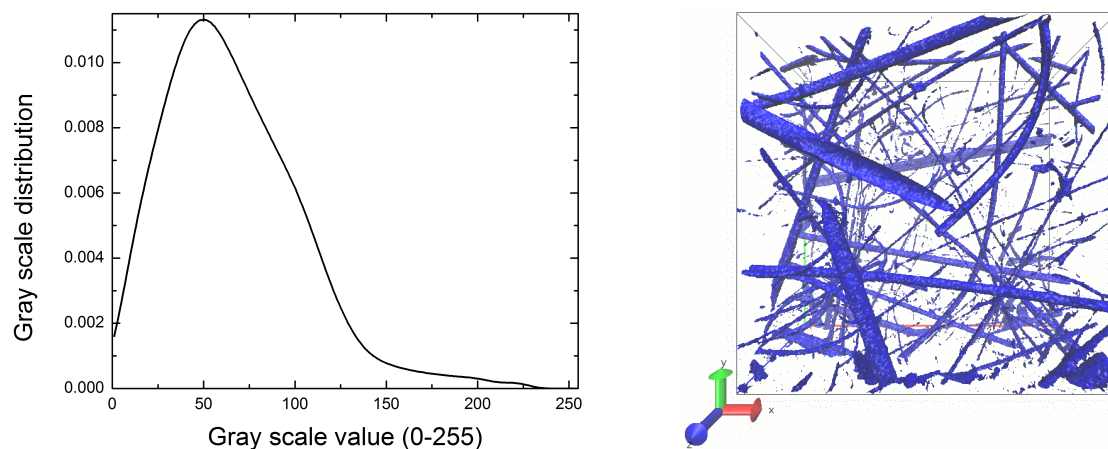

Fig.8 (a) Gray scale distribution of a sample image in Group D, and (b) A reconstructed sample image of BGF, Group D

The specific surface areas obtained by 3D image analysis of the CLSM data increase with decreasing mean fiber diameter (*c.f.* Table 2 and image analysis below) for all four groups. With the exception of Group D, however, the values obtained by 3D image analysis of the CLSM data are significantly larger than those measured by BET analysis of the adsorption isotherms. The good agreement between the S and S_{cyl} from the image analysis suggests that the discrepancy is not due to pixilation in the 3D images. Rather, there appears to be a real difference between the geometric surface area and that available for adsorption of krypton on the polyamides. The unusually large value of S obtained for Group B by 3D image analysis can be traced to background noise due to chromatic aberration during image acquisition.

30

Table 3 Results of 3D image analysis of CLSM data.

	Group A	Group B	Group C	Group D
Porosity ε (%)	93.2 ± 1.9	94.3 ± 0.4	N/A[a]	N/A[a]
Specific surface area, S (μm^{-1})	2.4 ± 0.2	4.6 ± 0.2	3.9 ± 0.3	4.9 [b]
Specific surface area, $S_{cyl}=<4/d>$ (μm^{-1})	2.3	4.1	3.96	4.56
Number average fiber diameter d (μm) [c]	1.99 ± 0.4	1.14 ± 0.6	1.09 ± 0.5	1.1 ± 0.2
Volume average pore diameter, s (μm) [d]	16.8 ± 6.0	13.3 ± 5.0	7.6 ± 3.0	14.7 ± 5.5
Fiber orientation factor, f	0.623 ± 0.009	0.627 ± 0.003	0.628 ± 0.001	0.614[b]
R_{th}^{max} (μm)	3.0	2.8	1.4	4.1
δ (μm) = $0.4R_{th}^{max}$	1.2	1.1	0.6	1.6
N_{gate}	2.1 ± 0.1	2.08 ± 0.04	2.02 ± 0.04	2.2
N_{cav}	5.0 ± 1.4	4.4 ± 0.8	4.8 ± 0.6	8.5

(a) Gravimetric porosity was used to determine grayscale threshold; see text for details.

(b) Only one sample analyzed.

(c) Error estimated as FWHM of $P(r^{mater})$.

(d) Error estimated as FWHM of $P(R_c^{pore})$.

4.4.2 Fiber diameter distribution

The area-weighted distributions of fiber radii $P\left(R_c^{mater}\right)$ for the four image groups are shown in Fig.9; the means and standard deviations of fiber diameter, computed according to Eq. (3) and (4), are reported in Table 3. For the fibers in Groups B and C, a second peak in $P\left(R_c^{mater}\right)$ appears for small values of $P\left(R_c^{mater}\right)$. This peak arises due to the acylindricity of the fibers, and has been neglected for subsequent characterization of fiber diameter (i.e. the average diameter computed by Eq. (4) does not include values for $R_c^{mater} < 0.3$ μm, corresponding to the local minimum in the distribution $P(R_b^{mater})$); this is very similar to the erosion operation with $R_{th} = 0.3$ μm in the material space. For comparison, the means and standard deviations of fiber diameter d_{SEM} obtained in the usual way from SEM images are reported in Table 2. Whereas analysis of SEM images tends to identify the largest dimension of the fiber cross-section, the use of covering spheres in 3D image analysis tends to identify the smallest dimension of the fiber cross-section. For cylindrical fibers, the two approaches should agree, but for acylindrical fibers, SEM estimates of fiber diameter should be larger than those obtained by the analysis reported here. For the data collected using the positive imaging technique (Groups A and C), the results are consistent with the SEM data - the fiber diameter of Group C is roughly half that of Group A, and the specific surface area is roughly double. The data collected by the negative imaging technique are noisier, resulting in a smaller estimate of fiber diameter d and a larger estimate of specific surface area S, than those obtained by SEM and BET, respectively. In addition, a second estimate of the specific surface area S_{cyl} can be obtained as the average, $<4/d>$, under the assumption that the fibers are perfectly cylindrical and non-intersecting; these values are also shown in Table 3. Comparison of S_{cyl} to S indicates that the latter yields an estimate consistent with the approximation that the fibers are cylindrical. It is noteworthy that the BGF is

characterized by a very polydisperse distribution of fiber diameters, which was already indicated by Fig.8 (b).
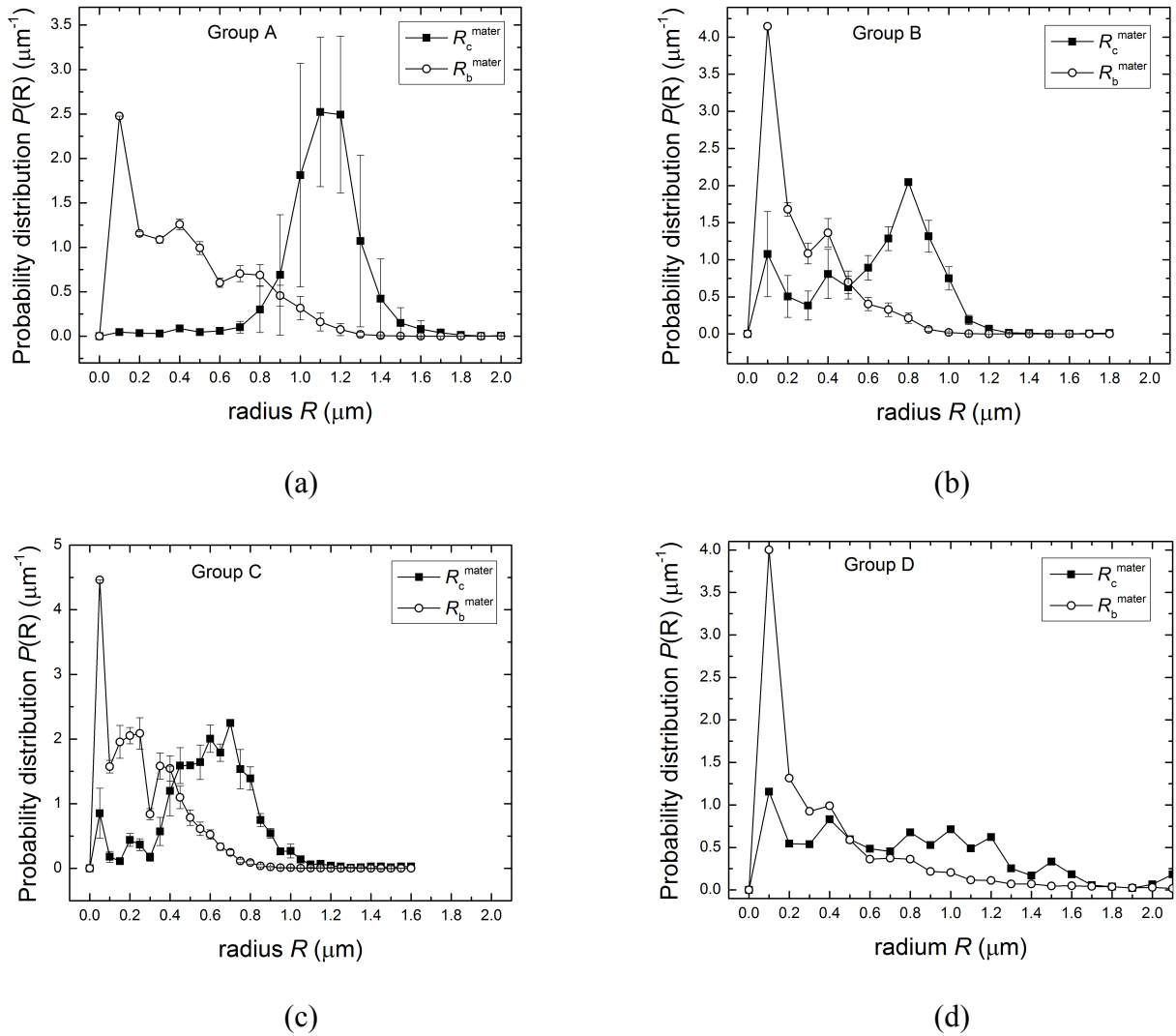

(a)

(b)

(c)

(d)

Fig.9 Boundary radius (R_b^{mater}) and covering radius (R_c^{mater}) distributions for the material space (i.e. fibers) in each sample group. (a) Group A; (b) Group B; (c) Group C; (d) Group D

4.4.3 Pore space structure

The pore space distributions $P\left(R_b^{pore}\right)$ and $P\left(R_c^{pore}\right)$ are shown in Fig.10 for Groups A and C. The distributions for the two sample groups are qualitatively similar; if R_b and R_c are re-scaled by a factor of ~2 (the ratio of the mean fiber diameters of the two sample groups), the similarity between the two sets of samples becomes evident. The average pore diameter $s = <2R_c>$ obtained from $P\left(R_c^{pore}\right)$ is reported in Table 3 for all four groups. For the electrospun mats (Groups A, B and C), s decreases as the fiber diameter decreases. This trend breaks down for the BGF (Group D), indicative of a difference in pore space structure that can probably be traced to the very broad fiber diameter distribution found for this group. The ratio of pore space diameter to fiber diameter (s/d) is about 8 for both Groups A and C. This value is consistent with the proportionality between pore dimension and fiber diameter reported previously by other methods [13, 48, 49], but its value is significantly higher than in previous reports. The discrepancy is likely a result of the limitations of liquid intrusion and extrusion methods for characterizing pore dimensions, mentioned already in the Introduction, and to differences in which moment of the pore size distribution is measured by each of those techniques.
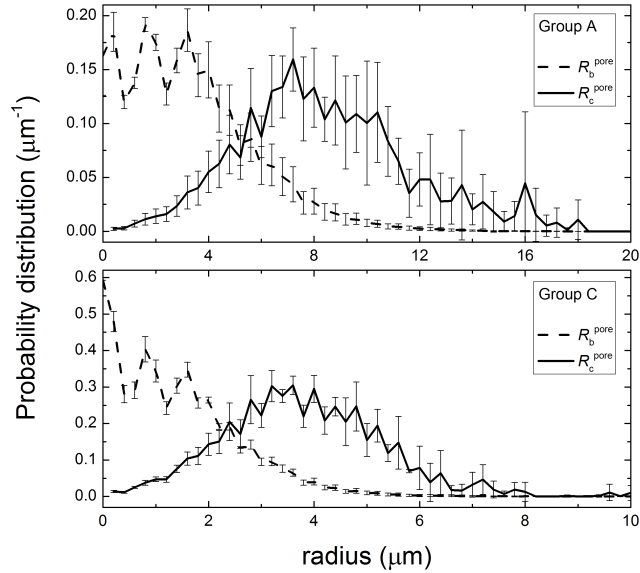
Fig.10 Boundary radius (R_b^{pore}) and covering radius (R_c^{pore}) distributions for the pore space of samples in Groups A and C. Note factor-of-2 difference in scaling of abscissas for the two plots

The sensitivity of these results to the values obtained for G_c was examined for the data of Group A. A 10% change in G_c resulted in a proportional change in estimates of solidity, specific surface area and fiber diameter distribution. However, the pore size distribution is relatively insensitive to such changes, primarily due to the high porosity of the system. Details may be found in the Supporting Information.

4.4.4 Fiber orientation distribution

Fig.11 shows the distribution of polar angles (θ, ϕ) for fiber orientation in Group A, measured using the 3D analysis. The θ angle is distributed narrowly around 90°, confirming the extent to which the fibers lie mostly in the x-y plane. The distribution of ϕ can be compared to the in-plane orientation distribution obtainable from SEM micrographs, also shown in Fig.11. The two

35

measurements for in-plane orientation distribution are qualitatively similar, although the analysis from CLSM data is more symmetric. The orientation factors, f_{SEM} and f, are reported in Table 2 and Table 3 for the SEM micrographs and the CLSM data, respectively. The f value given by the 3D data set is about 20% higher than the f_{SEM} value. The discrepancy could be due to the fact that the SEM analysis only counts fibers that can be imaged near the surface of the mat, and thus does not provide a complete representation of the overall fiber orientation.
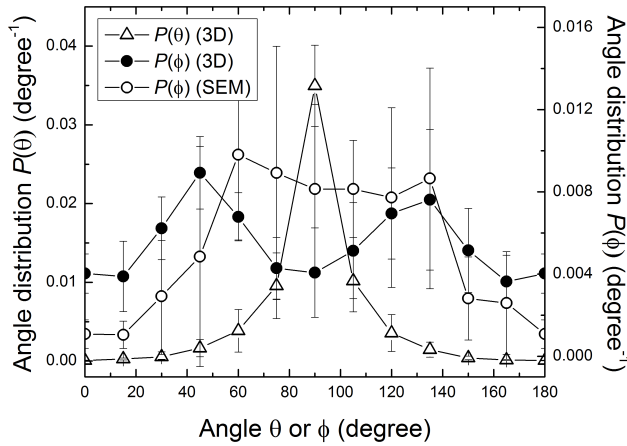

Fig.11 Fiber orientation distribution in polar angles (θ, ϕ) for image sample Group A measured from 3D image analysis and SEM images

4.4.5   Pore space topology

The specific Euler-Poincaré characteristic (χ_V) and its derivative with respect to R_{th} are plotted as functions of R_{th} for Group A in Fig.12 (a). χ_V increases with increasing R_{th} between 2 and 6 μm, indicative of the range of diameters of channels within the pore space. The maximum value of χ_V is ~200. The maximum of $d\chi_V/dR_{th}$ appears at $R_{th}^{max} = 3$ μm. Further insight into the Euler-Poincaré characteristic is provided by the plots of the number of isolated clusters of pore space

voxels, N, and the number of redundant connections, C, in Fig.12 (b). For small values of R_{th}, N is small while C is large, due to the highly interconnected nature of the pore space in an electrospun material. As R_{th} increases, connections are broken in the eroded space, resulting in larger numbers of isolated clusters. Beyond R_{th}~6 μm, the number of isolated clusters also begins to decline, as the erosion operation eliminates entire cavities as well as the connections between them.

The bubble point diameters (d_{bp}) and mean flow pore diameters (d_{mfp}) obtained by capillary flow porometry for each group are reported in Table 2. Comparison of these values with the geometric average pore diameters (s) and the characteristic channel diameters ($2R_{th}^{max}$) obtained by image analysis of the CLSM data and reported in Table 3 reveals that the values obtained by capillary flow porometry correspond to neither of the geometric results; both d_{mfp} and d_{bp} lie intermediate between s and $2R_{th}^{max}$ for all four groups. We interpret this as evidence for the highly acylindrical geometry of the channels within fibrous materials and in part a consequence of using the Young-Laplace equation to convert from pressure to channel diameter in these materials. More appropriate models for fibrous materials are available [50, 51]. Also, since the criterion $d\chi_v/dR_{th}$ reports the largest circle that can fit within a cross-sectional area of arbitrary shape, it tends towards smaller values of diameter compared to the "effective" cross-sectional area likely measured by the porometry experiment. Finally, it is also possible that fibers are displaced under the applied pressures used in capillary flow porometry, resulting in distortion of the morphology and a systematic bias towards larger values of diameter.
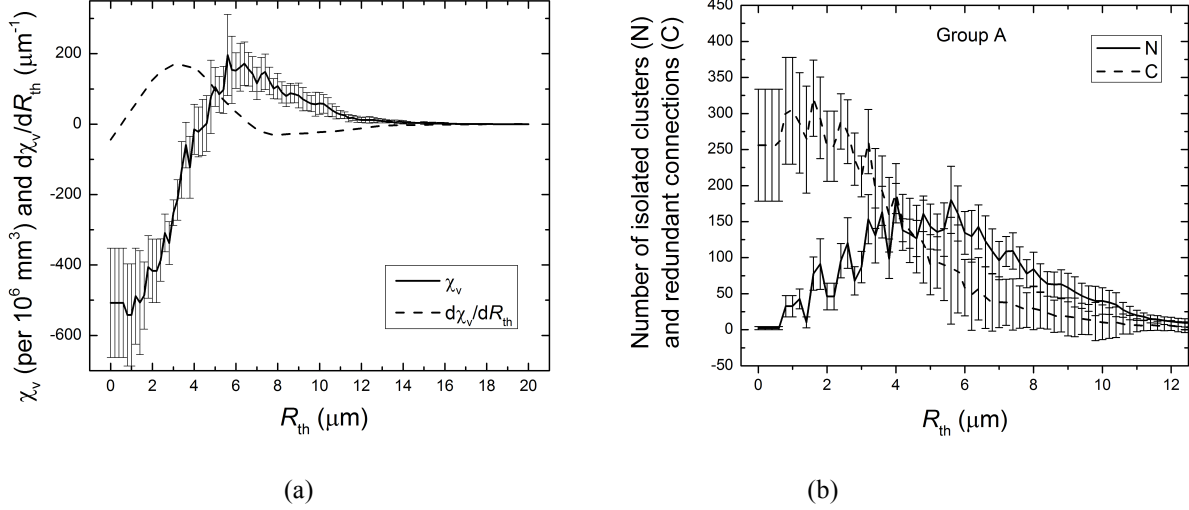
Fig.12 (a) Specific Euler-Poincaré characteristic χ_V and its derivative $d\chi_v / dR_{th}$ (smoothed) as functions of R_{th}, the radius of the spherical element used for the erosion operation, for Group A; (b) Number of isolated clusters, N, and number of redundant connections, C, as functions of R_{th}, for Group A

4.4.6 The pore space network

Judging from the width of the peak in $d\chi_v/dR_{th}$ in Fig.12 (a), the topology is sensitive to values of R_{th} as much as 2 μm on either side of $R_{th}^{max}=3$ μm. Thus, we identify $R_{th}^l = R_{th}^{max} - \delta$ with a lower bound of R_{th} where erosion first begins to affect the topology of the pore space, and $R_{th}^l = R_{th}^{max} + \delta$ with the upper bound of R_{th} beyond which further erosion has little effect on topology. Then, within the eroded space obtained using $R_b < R_{th}^l$, gate voxels are distinguished from cavity voxels by the criterion $R_c < R_{th}^u$. Finally, the gate and cavity voxels are clustered into distinct gates and cavities, respectively, and their connections (i.e. sharing of at least one common voxel side) are counted. Taking $R_{th}^{max} = 3$ μm for Group A, Fig.13(a) shows the numbers of distinct cavities and gates, obtained as functions of δ. Excluded from this plot are

those cavities for which the coordination number, N_{cav}, is zero (i.e. an isolated cluster of cavity voxels disconnnected from the network) and those gates for which the coordination number, N_{gate}, is less than or equal to one (i.e. an isolated or dead-end channel). Fig.13 (b) shows the coordination numbers for cavities and gates (*c.f.* Section 3.6), also excluding N_{cav}=0 and N_{gate}≤1. For 0.4<δ<1.4 μm, a picture consistent with the concept of a network of pores spaces is obtained. In this range of values, most gates join exactly two cavities (N_{gate}~2.0) and cavities are coordinated on average with one to five other cavities via shared gates (Table 3). For values of δ that are either smaller or larger than this range, the pore space is dominated by one or a few cavities or gates, respectively, and the network description is lost. Thus, to obtain a meaningful network description of the pore space in Group A, we conclude that gates, or channels, within the network are characterized by minimum radii between 0.4 and 1.4 μm.
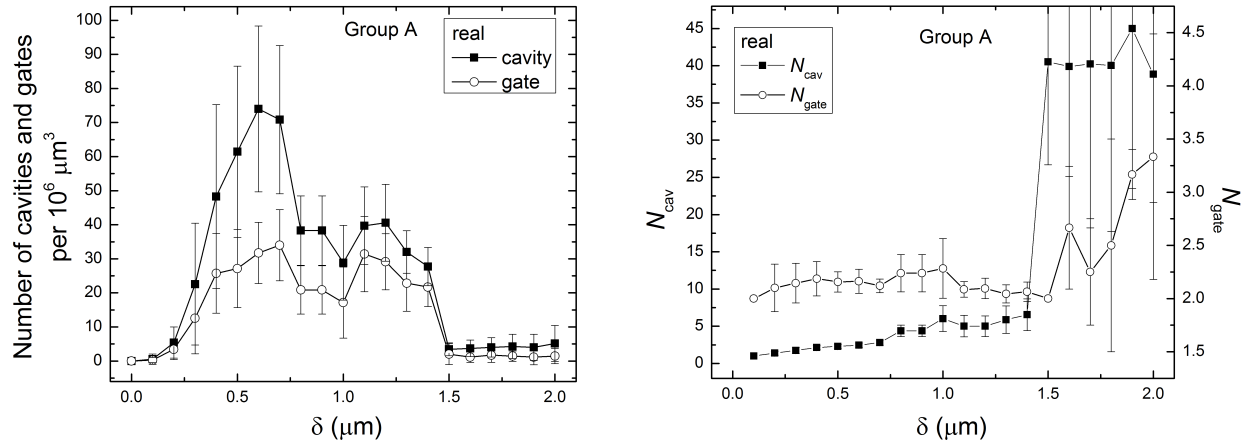

Fig.13 Group A: (a) numbers of distinct cavities and gates as functions of δ, for R_{th}^{max}=3.0 μm; (b) Coordination numbers of cavities and gates, N_{cav} and N_{gate}, respectively, as functions of δ. Cavities with N_{cav}=0 and gates with N_{gate}=0 or 1 are removed from statistics

Applying the same topological analysis to Group C (*c.f.* Supporting Information, Fig. S3) yields a picture similar to that for Group A. The R_{th}^{max} value obtained for Group C (*c.f.* Table 3) is about half that for Group A, in accord with the similar scaling of pore diameter *s* with fiber diameter *d*. The number densities of cavities and gates increase by about a factor of 8 compared to Group A, consistent with the finer subdivision of the pore space by a larger number of smaller diameter fibers. Nevertheless, the coordination of the network in Group C is very similar to that of Group A, with $N_{gate}\sim2$ and $2<N_{cav}<5$ for $0.2<\delta<0.6$. The metrics confirm the notion that the electrospun fiber samples in Group A and Group C are topologically similar, with comparable pore space connectivity, but differ by a scaling factor of the fiber diameter in both material and pore space dimensions.

By contrast, applying the topological analysis to the commercial borosilicate sample (Group D, Supporting Information, Fig. S4) suggests $R_{th} = 4.1$ µm, more similar to Group A, whereas the average fiber diameter $d = 1.1$ µm is more similar to Group C. As was observed for Group C, the number densities of cavities and gates are increased with respect to Group A, in accord with the presence of small diameter fibers within a broad distribution. The coordination number of gates remains $N_{gate}\sim2$ while the coordination number of cavities doubles to $2<N_{cav}<10$ for $0.5<\delta<1.6$. Despite the similar porosities and pore space dimensions for Groups A and D (*c.f.* Table 3), the topology of the pore space in the BGF samples of Group D is more "connected" than that of the electrospun nonwoven samples of either Group A or Group C.

5   Conclusions

In summary, CLSM with refractive index matching has been employed to obtain 3D data sets of electrospun PA6(3)T and borosilicate glass fiber mats. Two variations of the method, denoted "positive" and "negative" imaging are demonstrated, depending on whether the source of contrast lies within the material component or the pore space component. While the "positive" imaging approach is generally more robust and offers better signal-to-noise, the "negative" imaging approach offers greater flexibility with respect to imaging of porous materials that have not been formulated specifically for imaging purposes. 3D reconstructions of nonwoven fiber samples up to 100 μm in width and 50 μm in depth, resolving fibers with diameters as small as 0.6 μm, have thus been obtained.   For higher resolution, more advanced experimental methods or analysis tools are required. Tools are developed to analyze the structure of these 3D digitized reconstructions in terms of porosity, specific surface area, fiber diameter distribution, fiber orientation distribution, pore size distribution, topological connectivity, and network structure of the pore space. The analysis results are in reasonable agreement with other experimental measurements, where available, and yield additional insights into those measurements where discrepancies persist. Significantly, comparison of two sets of electrospun PA 6(3)T nonwoven fiber mats on the basis of material and pore space dimensions and topological measures of the pore space indicates that these materials are topologically similar, but differ morphologically by a scaling factor comparable to the ratio of their average fiber diameters. On the other hand, comparison of an electrospun PA 6(3)T nonwoven fiber mat with a borosilicate glass fiber material reveals differences in the topological nature for the two materials. The BGF has a broader distribution of fiber sizes, higher topological connectivity (as measure by the specific Euler-Poincaré characteristic), and a higher coordination number for cavities. To the best of our

knowledge, this work provides for the first time a detailed, quantitative characterization of both the morphology and topology of the pore space of a fibrous medium. The resulting metrics are purely geometrical, and do not rely on simplified material or pore shape models, or fluid interaction models such as the Young-Laplace equation, to convert transport measurements into geometrical properties.

References:

1. Baldwin, C.A., et al., *Determination and Characterization of the Structure of a Pore Space from 3D Volume Images.* Journal of Colloid and Interface Science, 1996. **181**(1): p. 79-92.
2. Auzerais, F.M., et al., *Transport in sandstone: A study based on three dimensional microtomography.* Geophysical Research Letters, 1996. **23**(7): p. 705-708.
3. Jones, J.R., et al., *Non-destructive quantitative 3D analysis for the optimisation of tissue scaffolds.* Biomaterials, 2007. **28**(7): p. 1404-1413.
4. Jaganathan, S., H. Vahedi Tafreshi, and B. Pourdeyhimi, *A realistic approach for modeling permeability of fibrous media: 3-D imaging coupled with CFD simulation.* Chemical Engineering Science, 2008. **63**(1): p. 244-252.
5. Levitz, P., *Toolbox for 3D imaging and modeling of porous media: Relationship with transport properties.* Cement and Concrete Research, 2007. **37**(3): p. 351-359.
6. Turner, M.L., et al., *Three-dimensional imaging of multiphase flow in porous media.* Physica A: Statistical Mechanics and its Applications, 2004. **339**(1–2): p. 166-172.
7. Kozeny, J., *Ueber kapillare Leitung des Wassers im Boden.* Sitzungsber Akad. Wiss., Wien, 1927. **136**(2a): p. 271-306.
8. Carman, P., *Fluid flow through granular beds.* Transactions of the Institution of Chemical Engineers, 1937. **15**: p. 150-166.
9. Fatt, I., *The Network Model of Porous Media. 1. Capillary Pressure Characteristics.* Transactions of the American Institute of Mining and Metallurgical engineers, 1956. **207**(7): p. 144-159.
10. Valvatne, P.H. and M.J. Blunt, *Predictive pore-scale modeling of two-phase flow in mixed wet media.* Water Resour. Res., 2004. **40**(7): p. W07406.
11. Chen, S. and G.D. Doolen, *LATTICE BOLTZMANN METHOD FOR FLUID FLOWS.* Annual Review of Fluid Mechanics, 1998. **30**(1): p. 329-364.
12. Cancedda, R., et al., *Tissue engineering and cell therapy of cartilage and bone.* Matrix Biology, 2003. **22**(1): p. 81-91.
13. Lowery, J.L., N. Datta, and G.C. Rutledge, *Effect of fiber diameter, pore size and seeding method on growth of human dermal fibroblasts in electrospun poly(-caprolactone) fibrous mats.* Biomaterials, 2010. **31**(3): p. 491-504.
14. Luu, Y.K., et al., *Development of a nanostructured DNA delivery scaffold via electrospinning of PLGA and PLA–PEG block copolymers.* Journal of Controlled Release, 2003. **89**(2): p. 341-353.
15. Liu, H., et al., *Polymeric Nanowire Chemical Sensor.* Nano Letters, 2004. **4**(4): p. 671-675.
16. Chen, L., et al., *Multifunctional Electrospun Fabrics via Layer-by-Layer Electrostatic Assembly for Chemical and Biological Protection.* Chemistry of Materials, 2010. **22**(4): p. 1429-1436.
17. Burger, C., B.S. Hsiao, and B. Chu, *NANOFIBROUS MATERIALS AND THEIR APPLICATIONS.* Annual Review of Materials Research, 2006. **36**(1): p. 333-368.

18. Pai, C.-L., M.C. Boyce, and G.C. Rutledge, *Mechanical properties of individual electrospun PA 6(3)T fibers and their variation with fiber diameter.* Polymer, 2011. **52**(10): p. 2295-2301.

19. Tomba, E., et al., *Artificial Vision System for the Automatic Measurement of Interfiber Pore Characteristics and Fiber Diameter Distribution in Nanofiber Assemblies.* Industrial & Engineering Chemistry Research, 2010. **49**(6): p. 2957-2968.

20. Rutledge, G.C., J.L. Lowery, and C.L. Pai, *Characterization by Mercury Porosimetry of Nonwoven Fiber Media with Deformation.* Journal of Engineered Fibers and Fabrics, 2009. **4**(3): p. 1-13.

21. Jena, A. and K. Gupta, *Pore Volume of Nanofiber Nonwovens.* International Nonwovens Journal, 2005. **14**(2).

22. Sampson, W. and S. Urquhart, *The contribution of out-of-plane pore dimensions to the pore size distribution of paper and stochastic fibrous materials.* Journal of Porous Materials, 2008. **15**(4): p. 411-417.

23. Eichhorn, S.J. and W.W. Sampson, *Relationships between specific surface area and pore size in electrospun polymer fibre networks.* Vol. 7. 2010. 641-649.

24. Ho, S.T. and D.W. Hutmacher, *A comparison of micro CT with other techniques used in the characterization of scaffolds.* Biomaterials, 2006. **27**(8): p. 1362-1376.

25. Stachewicz, U., et al., *Manufacture of Void-Free Electrospun Polymer Nanofiber Composites with Optimized Mechanical Properties.* ACS Applied Materials & Interfaces, 2012. **4**(5): p. 2577-2582.

26. Sarada, T., L.C. Sawyer, and M.I. Ostler, *Three dimensional structure of celgard® microporous membranes.* Journal of Membrane Science, 1983. **15**(1): p. 97-113.

27. Bagherzadeh, R., et al., *Three-dimensional pore structure analysis of Nano/Microfibrous scaffolds using confocal laser scanning microscopy.* Journal of Biomedical Materials Research Part A, 2013. **101A**(3): p. 765-774.

28. Thibault, X. and J.-F. Bloch, *Structural Analysis by X-Ray Microtomography of a Strained Nonwoven Papermaker Felt.* Textile Research Journal, 2002. **72**(6): p. 480-485.

29. Arns, C., et al., *Computation of linear elastic properties from microtomographic images: Methodology and agreement between theory and experiment.* Geophysics, 2002. **67**(5): p. 1396-1405.

30. Cox, G. and C.J.R. Sheppard, *Practical limits of resolution in confocal and non-linear microscopy.* Microscopy Research and Technique, 2004. **63**(1): p. 18-22.

31. Choong, L., et al., *Compressibility of electrospun fiber mats.* Journal of Materials Science, 2013. 48(22): p. 7827-7836.

32. Jähne, B., *Digital image processing.* 6th rev. and extended ed. 2005, Berlin: New York :Springer. xiii, 607 p.

33. Toll, S. and J.A.E. Manson, *Elastic Compression of a Fiber Network.* Journal of Applied Mechanics, 1995. **62**(1): p. 223-226.

34. Heller, W., *Remarks on Refractive Index Mixture Rules.* The Journal of Physical Chemistry, 1965. **69**(4): p. 1123-1129.

35. Gooch, J.W., *Encyclopedic Dictionary of Polymers.* 2. ed. 2011, New York, NY: Springer Science+Business Media, LLC.

36. *http://www.filmetrics.com/refractive-index-database/BSG/Borosilicate-Glass-Microscope-Slide.* [accessed Aug.25, 2014].

37. Schindelin, J., et al., *Fiji: an open-source platform for biological-image analysis.* Nat Meth, 2012. **9**(7): p. 676-682.
38. du Roscoat, S.R., J.-F. Bloch, and X. Thibault, *Synchrotron radiation microtomography applied to investigation of paper.* Journal of Physics D: Applied Physics, 2005. **38**(10A): p. A78.
39. Pfeifer, P., et al., *Structure analysis of porous solids from preadsorbed films.* Langmuir, 1991. **7**(11): p. 2833-2843.
40. Gelb, L.D. and K.E. Gubbins, *Pore Size Distributions in Porous Glasses: A Computer Simulation Study.* Langmuir, 1999. **15**(2): p. 305-308.
41. Serra, J.P., *Image analysis and mathematical morphology.* 1982, London ;New York: Academic Press.
42. Ohser, J. and W. Nagel, *The estimation of the Euler-Poincare characteristic from observations on parallel sections.* Journal of Microscopy, 1996. **184**(2): p. 117-126.
43. Nagel, Ohser, and Pischang, *An integral-geometric approach for the Euler–Poincaré characteristic of spatial images.* Journal of Microscopy, 2000. **198**(1): p. 54-62.
44. Vogel, H.J., *Morphological determination of pore connectivity as a function of pore size using serial sections.* European Journal of Soil Science, 1997. **48**(3): p. 365-377.
45. Kanit, T., et al., *Determination of the size of the representative volume element for random composites: statistical and numerical approach.* International Journal of Solids and Structures, 2003. **40**(13–14): p. 3647-3679.
46. Kanit, T., et al., *Apparent and effective physical properties of heterogeneous materials: Representativity of samples of two materials from food industry.* Computer Methods in Applied Mechanics and Engineering, 2006. **195**(33–36): p. 3960-3982.
47. du Roscoat, S.R., et al., *Estimation of microstructural properties from synchrotron X-ray microtomography and determination of the REV in paper materials.* Acta Materialia, 2007. **55**(8): p. 2841-2850.
48. Wang, R., et al., *Electrospun nanofibrous membranes for high flux microfiltration.* Journal of Membrane Science, 2012. **392**: p. 167-174.
49. Pham, Q.P., U. Sharma, and A.G. Mikos, *Electrospun Poly(ε-caprolactone) Microfiber and Multilayer Nanofiber/Microfiber Scaffolds: Characterization of Scaffolds and Measurement of Cellular Infiltration.* Biomacromolecules, 2006. **7**(10): p. 2796-2805.
50. Rijke, A.M., *WETTABILITY AND PHYLOGENETIC DEVELOPMENT OF FEATHER STRUCTURE IN WATER BIRDS.* Journal of Experimental Biology, 1970. **52**(2): p. 469-479.
51. Tuteja, A., et al., *Robust omniphobic surfaces.* Proceedings of the National Academy of Sciences, 2008. **105**(47): p. 18200-18205.